information

MDPI

Article

Reduced-Order Model of Coal Seam Gas Extraction Pressure Distribution Based on Deep Neural Networks and Convolutional Autoencoders

Tianxuan Hao [1,2,3], Lizhen Zhao [1,2,*], Yang Du [1,2,*], Yiju Tang [4], Fan Li [1,2], Zehua Wang [1,2] and Xu Li [1,2]

[1] College of Safety Science and Engineering, Henan Polytechnic University, Jiaozuo 454000, China
[2] State Key Laboratory Cultivation Base for Gas Geology and Gas Control, Henan Polytechnic University, Jiaozuo 454000, China
[3] State Collaborative Innovation Center of Coal Work Safety and Clean-Efficiency Utilization, Jiaozuo 454000, China
[4] School of Municipal and Environmental Engineering, Henan University of Urban Construction, Pingdingshan 467036, China
* Correspondence: 112001010004@home.hpu.edu.cn (L.Z.); 112001010002@home.hpu.edu.cn (Y.D.)

Abstract: There has been extensive research on the partial differential equations governing the theory of gas flow in coal mines. However, the traditional Proper Orthogonal Decomposition–Radial Basis Function (POD-RBF) reduced-order algorithm requires significant computational resources and is inefficient when calculating high-dimensional data for coal mine gas pressure fields. To achieve the rapid computation of gas extraction pressure fields, this paper proposes a model reduction method based on deep neural networks (DNNs) and convolutional autoencoders (CAEs). The CAE is used to compress and reconstruct full-order numerical solutions for coal mine gas extraction, while the DNN is employed to establish the nonlinear mapping between the physical parameters of gas extraction and the latent space parameters of the reduced-order model. The DNN-CAE model is applied to the reduced-order modeling of gas extraction flow–solid coupling mathematical models in coal mines. A full-order model pressure field numerical dataset for gas extraction was constructed, and optimal hyperparameters for the pressure field reconstruction model and latent space parameter prediction model were determined through hyperparameter testing. The performance of the DNN-CAE model order reduction algorithm was compared to the POD-RBF model order reduction algorithm. The results indicate that the DNN-CAE method has certain advantages over the traditional POD-RBF method in terms of pressure field reconstruction accuracy, overall structure retention, extremum capture, and computational efficiency.

Keywords: coal mine; gas extraction; gas flow model; reduced-order model; deep neural networks; convolutional autoencoders

check for updates

Citation: Hao, T.; Zhao, L.; Du, Y.; Tang, Y.; Li, F.; Wang, Z.; Li, X. Reduced-Order Model of Coal Seam Gas Extraction Pressure Distribution Based on Deep Neural Networks and Convolutional Autoencoders. *Information* **2024**, *15*, 733. https://doi.org/10.3390/info15110733

Academic Editor: Gabriele Gianini

Received: 23 September 2024
Revised: 7 November 2024
Accepted: 14 November 2024
Published: 16 November 2024

1. Introduction

Coal serves as an indispensable safeguard energy source within China. However, as the depth of coal mining increases, gas disasters have become increasingly severe, posing significant threats to the safety of coal mine production. The concept of a digital twin for mines offers the potential to ensure sustainable, efficient, and safe coal mining operations. A critical component of this digital twin concept is the theory of gas flow within coal seams. Consequently, research on gas flow theory has been extensive [1,2]. This body of work includes studies on the evolution of coal and rock permeability and gas flow under the influences of mining activities, stress, moisture, and permeability enhancement technologies [3–9]. These studies have led to the development of new coal seam gas flow models [10–15], which have undergone reliability validation. Further research has integrated practical engineering data to perform numerical calculations on coal seam gas flow models, guiding and optimizing engineering design [16–18]. These advancements have significantly improved production efficiency and safety in coal mining enterprises.

Currently, numerical computation methods are widely used to solve multi-physical models. However, these methods often require significant hardware performance and can take a substantial amount of time to compute, ranging from several hours to days. This poses certain limitations for their application in digital twin technology [19]. Digital twins require models that can provide accurate and rapid real-time solutions to monitor equipment status. Model order reduction (MOR) is a key technique used to accelerate the computation of mathematical models. MOR aims to provide a low-dimensional approximation of time-varying, multi-dimensional physical processes, thereby reducing the computational dimensionality, decreasing computation time, and lessening CPU load. Among the popular methods currently in use is the combination of Proper Orthogonal Decomposition and Radial Basis Function (POD-RBF) neural networks. This approach has been extensively studied and applied in practical engineering and digital twin applications [20–23]. For instance, Zendaki et al. employed the POD-RBF algorithm as a substitute for finite element calculations, enabling rapid computations of surface settlement, strain in existing structures, and stress and deformation of tunnel linings during tunneling operations [24]. Rao described a reduced-order model based on POD-RBF for the inverse estimation of model parameters such as material properties and boundary conditions in fluid flow and thermal systems [25]. Shen et al. proposed the use of POD-RBF to analyze the impact of uncertain parameters on the response of cracked structures [26,27]. Zhang et al. introduced the application of POD-RBF reduced-order models for predicting acoustic fields in infinite domains, facilitating the rapid reconstruction of acoustic fields for complex models [28].

However, when applied to the residual gas pressure field after gas extraction in coal mines, high-dimensional pressure field data lead to excessive computational demands for the POD-RBF method, resulting in prolonged computation times. In contrast, deep learning methods exhibit strong capabilities in capturing nonlinear features and demonstrate high computational efficiency, offering significant potential for practical engineering applications. Therefore, this paper proposes a reduced-order modeling approach for coal mine gas extraction based on the DNN and CAE. The CAE is utilized to compress and reconstruct the full-order numerical solutions of coal mine gas extraction, while the DNN is employed to establish a nonlinear mapping relationship between the physical parameters of gas extraction and the latent space parameters of the reduced-order model. This work aims to provide insights and guidance for the research and application of digital twins and model order reduction in mining.

2. Materials and Methods

2.1. Full-Order Modeling of Coal Seam Gas Extraction

Previous research has established that the physical process of coal mine gas extraction can be represented as a coupled process involving gas flow and diffusion fields and the stress field of the coal–rock mass. During coal seam gas extraction, the primary modes of gas migration include seepage and diffusion. The main factors influencing gas migration are the initial gas pressure in the coal seam and the permeability of the coal seam's porous medium. The gas pressure in the coal seam determines the pressure gradient between the coal seam and the boreholes, which in turn affects the effective stress of the coal seam, thereby influencing its permeability [29–32].

Gas extraction may disrupt the gas pressure equilibrium between the fracture system and the coal matrix, causing the adsorbed gas to diffuse from the coal matrix into the fractures. The rate of change in gas mass in the coal matrix is expressed as follows:

$$\frac{\partial m_{\mathrm{m}}}{\partial t} = -\frac{M_{\mathrm{c}}}{\tau RT}(p_{\mathrm{m}} - p_{\mathrm{f}}) \tag{1}$$

where t is time, M_c represents the molar mass of gas, τ is the adsorption time, R is the gas constant, T is the absolute temperature, p_m is the gas pressure in the coal matrix, and p_f denotes gas pressure in fractures.

The governing equation for the variation in gas pressure in the coal matrix over time is as follows:

$$\frac{\partial p_\mathrm{m}}{\partial t} = -\frac{V_\mathrm{M}(p_\mathrm{m}-p_\mathrm{f})(p_\mathrm{m}+P_\mathrm{L})^2}{\tau V_\mathrm{L} RTP_\mathrm{L}\rho_\mathrm{c} + \tau\phi_\mathrm{m} V_\mathrm{M}(p_\mathrm{m}+P_\mathrm{L})^2} \tag{2}$$

where ϕ_m is the porosity of the coal matrix, V_M represents the molar volume of gas, V_L denotes the Langmuir volume constant, P_L denotes the Langmuir pressure constant, and ρ_c indicates the density of the coal matrix.

The governing equation for gas flow in the coal seam can be expressed as follows:

$$\phi_\mathrm{f}\frac{\partial \rho_\mathrm{f}}{\partial t} + \rho_\mathrm{f}\frac{\partial \phi_\mathrm{f}}{\partial t} + \nabla\rho_\mathrm{g}\left(-\frac{k_\mathrm{f}}{\mu}\nabla p_\mathrm{f}\right) = \frac{M_\mathrm{c}}{\tau RT}(p_\mathrm{m}-p_\mathrm{f})(1-\phi_\mathrm{f}) \tag{3}$$

where ϕ_f represents the coal porosity, k_f represents the gas permeability, μ is the kinetic viscosity coefficient of gas, p_f denotes the gas pressure in fractures, and ρ_g indicates the gas density in fractures.

The effective stress in coal is influenced by in situ stress, gas pressure within the coal, and the adsorption and desorption of gas. The response of effective stress in coal can be represented by the following equation:

$$Gu_\mathrm{i,jj} + \frac{G}{1-2v}u_\mathrm{j,ji} - \alpha p_\mathrm{f,i} - \beta p_\mathrm{m,i} - K\varepsilon_\mathrm{s,j} + F_\mathrm{i} = 0 \tag{4}$$

where G is the shear modulus, v is the Poisson ratio of coal, α and β denote the Biot coefficients, K indicates the volumetric modulus of coal, ε_s represents the adsorption strain of coal, u_ij and u_ji are the displacement components, and F_i represents the volume force component.

The permeability of coal is primarily influenced by the effective stress in the coal, gas pressure within the coal seam, and the adsorption and desorption of gas. Since the cubic law is satisfied between porosity and permeability [33], the dynamic evolution equation for the permeability of the coal seam can be expressed as follows:

$$\frac{k}{k_0} = \left(\frac{\phi_\mathrm{f}}{\phi_\mathrm{f0}}\right)^3 = \left(\frac{1}{\phi_\mathrm{f0}} - \frac{1-\phi_\mathrm{f0}}{\phi_\mathrm{f0}(1+\varepsilon_\mathrm{V})}\left(1-\frac{\alpha}{K_\mathrm{s}}\Delta p_\mathrm{f} + \Delta\varepsilon_\mathrm{s}\right)\right)^3 \tag{5}$$

where k is the coal permeability, k_0 is the initial value of k, ϕ_f0 represents the initial value of ϕ_f, ε_V is the volumetric strain of the coal matrix, and K_s is the skeleton volume modulus of coal.

Figure 1 illustrates the coupling relationship between the physical fields. According to the modeling requirements of this paper and systems theory, the input variables of this system are initial coal seam gas pressure, initial permeability of coal seam, and extraction time, and the output variables are the gas extraction flow rate, gas extraction concentration, and residual gas pressure field of coal seam.

As shown in Figure 2, a specific simulation range with a length of 50 m and a width of 50 m was selected for the numerical simulation of regional gas extraction. The simulation was subjected to an in situ stress of 17 MPa, calculated based on the burial depth of the coal seam. For gas flow simulation, an extraction negative pressure of 17 kPa was applied at the borehole boundary within the coal seam, while the other boundaries were set as no-flow boundaries. The initial gas pressure was set to 1.5 MPa, with a borehole diameter of 103 mm. Additional detailed parameters are provided in Table 1.

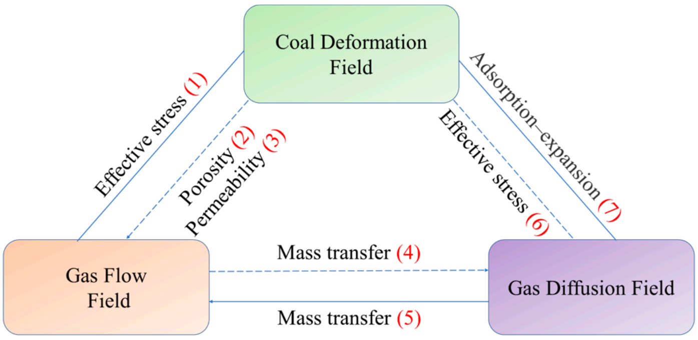

Field Equation

$$Gu_{i,jj}+\frac{G}{1-2v}u_{j,ji}\underbrace{-\alpha p_{f,i}}_{(1)}\underbrace{-\beta p_{m,i}}_{(6)}\underbrace{-K\varepsilon_{s,j}}_{(7)}+F_{,i}=0$$

$$\underbrace{\phi_{\mathrm{f}}\frac{\partial\rho_{\mathrm{f}}}{\partial t}+\rho_{\mathrm{f}}\frac{\partial\phi_{\mathrm{f}}}{\partial t}}_{(2)}+\underbrace{\nabla\rho_{\mathrm{g}}\left(-\frac{k_{\mathrm{f}}}{\mu}\nabla p_{\mathrm{f}}\right)}_{(3)}=\underbrace{\frac{M_{\mathrm{c}}}{\tau RT}\left(p_{\mathrm{m}}-p_{\mathrm{f}}\right)\left(1-\phi_{\mathrm{f}}\right)}_{(4)}$$

$$\frac{\partial p_{\mathrm{m}}}{\partial t}=-\frac{V_{\mathrm{M}}\left(p_{\mathrm{m}}-p_{\mathrm{f}}\right)\left(p_{\mathrm{m}}+P_{\mathrm{L}}\right)^{2}}{\tau V_{\mathrm{L}}RTP_{\mathrm{L}}\rho_{\mathrm{c}}+\tau\phi_{\mathrm{m}}V_{\mathrm{M}}\left(p_{\mathrm{m}}+P_{\mathrm{L}}\right)^{2}}\qquad\frac{\partial m_{\mathrm{m}}}{\partial t}=\underbrace{-\frac{M_{\mathrm{c}}}{\tau RT}\left(p_{\mathrm{m}}-p_{\mathrm{f}}\right)}_{(5)}$$

Coupling Term

$$\frac{k}{k_0}=\frac{\phi_{\mathrm{f}0}}{\phi_{\mathrm{f}0}}=\left(\frac{1}{\phi_{\mathrm{f}0}}-\frac{1-\phi_{\mathrm{f}0}}{\phi_{\mathrm{f}0}\left(1+\varepsilon_{\mathrm{V}}\right)}\left(1-\frac{\alpha}{K_{\mathrm{s}}}\Delta p_{\mathrm{f}}+\Delta\varepsilon_{\mathrm{s}}\right)\right)^{3}$$

Figure 1. Physical field coupling relation of coal seam gas extraction flow model.

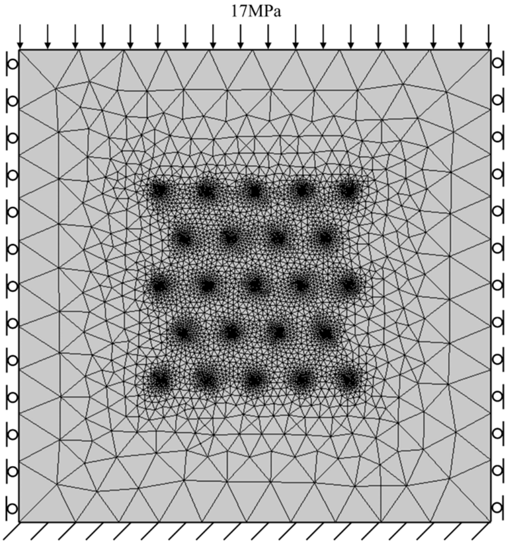

Figure 2. Geometric modeling for numerical simulation of gas extraction.

Table 1. The physical parameters of finite element numerical simulation.

Parameters	Values
Molar mass of gas, M_c	0.016 kg/mol
Molar gas constant, R	8.3143 J/(mol·K)
Coal temperature, T	300 K
Initial fracture porosity of coal, ϕ_{f0}	0.012
Gas Langmuir volumetric strain constant, ε_L	0.0128
Initial permeability of coal seam, k_0	3×10^{-17} m^2
Poisson’s ratio of coal seam, v	0.339
Molar volume of gas at standard conditions, V_m	22.4 L/mol

Table 1. *Cont.*

Parameters	Values
Kinetic viscosity coefficient of gas, μ	1.08×10^{-5} Pa·s
Langmuir pressure constant for gas, P_{L}	1×10^{6} Pa
Langmuir volume constant for gas, V_{L}	0.02 m^3/kg
Apparent density of coal seam, ρ_{c}	1250 kg/m^3
Adsorption time, τ	9.2 d
Modulus of elasticity of coal seam, E	2.7×10^{9} Pa

2.2. Convolutional Autoencoder-Based Reconstruction Model for Coal Seam Gas Extraction Pressure Field

An autoencoder is an unsupervised learning algorithm with a specialized neural network structure for encoding and decoding, making it suitable for tasks such as data compression, feature extraction, data reconstruction, and matrix factorization. It is widely used in fields like image reconstruction, image restoration, anomaly detection, image denoising, and image segmentation. Convolutional autoencoders, which replace the fully connected layers of traditional autoencoders with convolutional layers, significantly enhance the ability to capture spatial information. This makes convolutional autoencoders more capable of handling complex image processing tasks compared to ordinary autoencoders.

In this study, a convolutional autoencoder was employed as the reconstruction algorithm for the coalbed methane drainage seepage field, leading to the development of a convolutional autoencoder-based model for reconstructing the coalbed methane drainage seepage field. The model's structure, as shown in Figure 3, consists mainly of two parts: an encoder and a decoder. The network follows a symmetrical structure, with the left side comprising the encoder, which includes convolutional layers, max-pooling downsampling layers, and fully connected layers. The right side consists of the decoder, featuring deconvolutional networks, upsampling layers, and fully connected layers. The encoder takes a 64 × 64 single-channel input, with feature map sizes progressively decreasing: $64 \times 64 > 32 \times 32 > 16 \times 16 > 8 \times 8 > 4 \times 4$. It then flattens into a one-dimensional array of length of 16, which is further compressed into two latent space features through three fully connected layers. The decoder's structure mirrors that of the encoder. It starts by inputting the two latent space features into three fully connected layers, expanding into a one-dimensional array of length of 4. The feature map sizes then progressively increase: $2 \times 2 > 4 \times 4 > 8 \times 8 > 16 \times 16 > 32 \times 32 > 64 \times 64$. The final output is a coalbed methane drainage pressure field map of the same dimensions as the input. This network architecture combines the feature extraction capabilities of convolutional networks with the spatial reconstruction abilities of deconvolutional networks, making it highly suitable for pressure field reconstruction tasks that require precise pixel-level predictions.

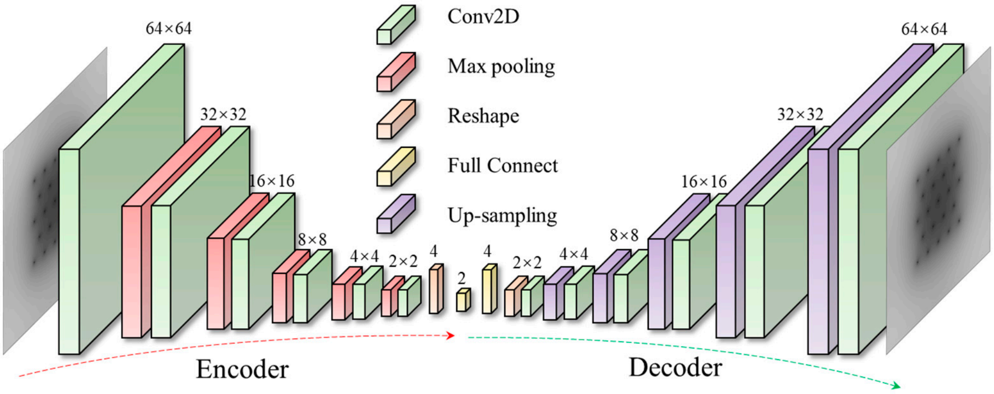

Figure 3. CAE model structure for reconfiguration of pressure field in coal seam gas extraction.

2.3. Deep Neural Network-Based Prediction Model for Potential Spatial Parameters

To incorporate three crucial parameters of coal mine methane extraction and establish a nonlinear mapping relationship between these parameters and the latent space parameters of the coalbed methane drainage pressure field, this study developed a highly adaptable deep neural network capable of handling various complex issues. The network consists of an input layer, an output layer, and three hidden layers, as illustrated in Figure 4. Each node in a given layer is fully connected to all nodes in the subsequent layer, with inter-layer connections depicted in different colors for clarity. The input layer consists of five nodes: x_1, x_2, x_3, x_4, x_5. The first hidden layer comprises 50 nodes (${h_1}^{(1)}$ to ${h_{50}}^{(1)}$), the second hidden layer contains 25 nodes (${h_1}^{(2)}$ to ${h_{25}}^{(2)}$), and the third hidden layer has 10 nodes (${h_1}^{(3)}$ to ${h_{10}}^{(3)}$). The output layer includes 2 nodes. The number of nodes in the input layer is typically determined by the number of features, while the number of nodes in the output layer depends on the output. For the hidden layers, it is recommended to start with a smaller network, beginning with 5 neurons and a single hidden layer, and gradually increase the number of nodes until the model's performance no longer shows a significant improvement.

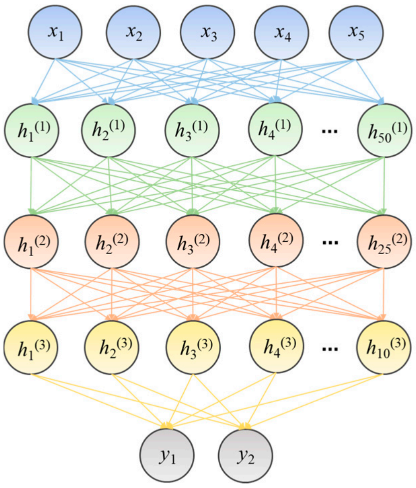

Figure 4. Structure of the DNN model for predicting patent space parameters of methane extraction pressure field.

2.4. Grid Search Method

This study employs a grid search method with cross-validation to optimize and improve the network. The grid search method can be divided into two parts: search and cross-validation. In grid search, various parameter combinations are exhaustively traversed; hence, it is also referred to as exhaustive search. Cross-validation is a statistical method that involves partitioning a dataset into smaller subsets. K-fold cross-validation is a widely used form of cross-validation. This study employs a 5-fold cross-validation approach, wherein the complete dataset is randomly partitioned into five subsets of equal size. In each iteration, four subsets are utilized as the training set, while the remaining subset serves as the test set. This process is repeated five times, and the average accuracy is computed to serve as the final evaluation metric for the model.

2.5. DNN-CAE-Based Reduced-Order Model for Coal Seam Gas Extraction

This section primarily presents the DNN-CAE reduced-order model for coalbed methane extraction, which integrates convolutional autoencoders (CAEs) and deep neural networks (DNNs). The complete workflow, from full-order mathematical modeling to reduced-order prediction models, combining physical modeling with data-driven approaches, is illustrated in Figure 5, and the framework is shown in Figure 6.

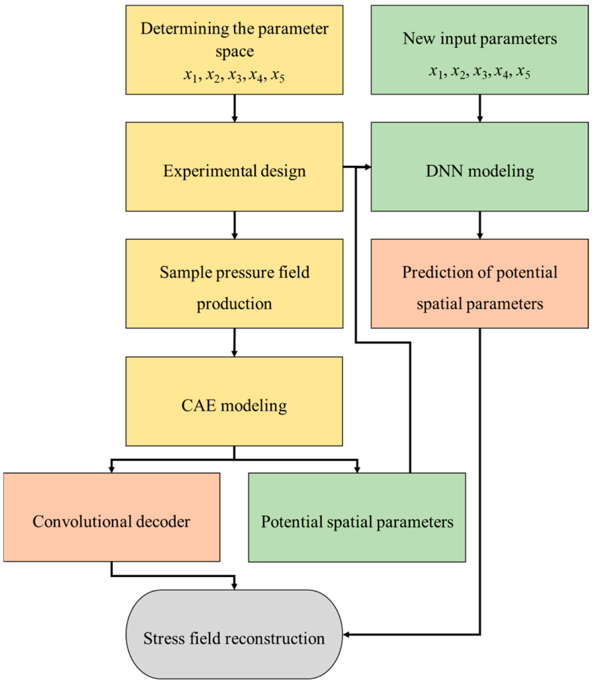

Figure 5. DNN-CAE model construction process.

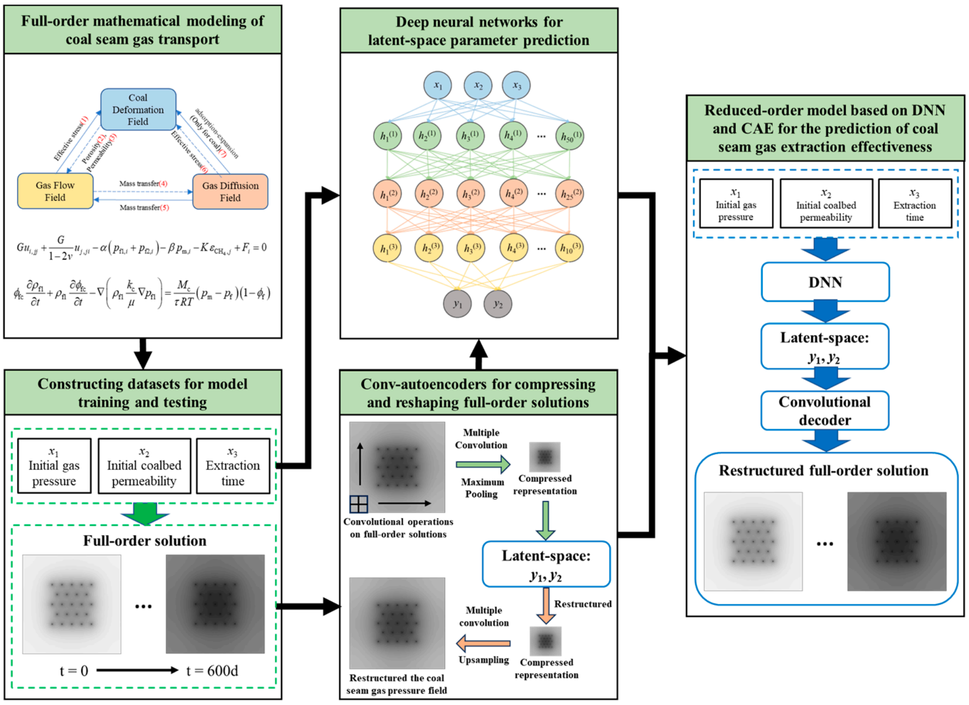

Figure 6. DNN-CAE-based reduced-order model for coal seam gas extraction.

(1) Full-order mathematical modeling of coalbed methane extraction: Establish a set of partial differential equations representing the coalbed methane extraction process, including the gas migration field, effective stress field, and permeability evolution field. This modeling provides the theoretical foundation for subsequent numerical computations and dataset construction.

(2) Dataset construction: Construct training and testing datasets for the convolutional autoencoder (CAE) and deep neural network (DNN) models. As an unsupervised learning method, the CAE dataset consists of full-order numerical solutions for coalbed

methane extraction. The input for the DNN model includes factors affecting coalbed methane extraction, such as initial gas pressure, initial coal seam permeability, and mining time.

(3) Pressure field reconstruction model construction: Section 2.2 describes the CAE established in this study for compressing and reconstructing the full-order numerical solutions of coalbed methane extraction. The process begins with inputting the full-order numerical solution into the CAE. Through multi-scale convolution and upsampling operations, the full-order solution is compressed into a lower-dimensional latent space and then reconstructed to its original dimension. The reconstructed solution is compared with the full-order numerical solution to calculate the error, and the CAE is continuously optimized using the Adam optimization method.

(4) Latent space parameter prediction model construction: Section 2.3 introduces the DNN developed to predict latent space parameters. This network establishes a nonlinear mapping relationship between the physical parameters of coalbed methane extraction and the latent space parameters of the reduced-order model. The network takes coalbed methane extraction physical parameters as the input and, through multiple fully connected neural network layers, outputs the latent space parameters of the reduced-order model. The Adam optimization method is also used to optimize the deep fully connected neural network.

(5) Construction of the reduced-order model for coalbed methane extraction: Integrating the deep fully connected neural network and CAE to achieve a reduced-order model for the full-order mathematical model of coalbed methane extraction. The model takes gas extraction parameters as the input, predicts latent space parameters using the deep fully connected neural network, and then reconstructs the full-order solution using the convolutional decoder.

3. Experiments

3.1. Datasets

Based on previous research on the factors influencing gas extraction [34,35], this study designed the parameter settings for the full-order numerical model of coalbed methane extraction, as shown in Table 2.

Table 2. Parameter settings for numerical calculation of the full-order model.

Influencing Factors	Variable Name	Unit	Value			
Initial coal seam gas pressure	x_1	MPa	1	2	3	4
Initial permeability of coal seam	x_2	10^{-17} m^2	1	2	3	4
Extraction time	x_3	day	1, 11, 21, 31, …, 301			

This study focuses on three primary influencing factors: x_1 initial coalbed methane pressure, x_2 initial permeability, and x_3 extraction time. Initial coalbed methane pressure x_1 represents the methane pressure in the coalbed prior to extraction. It significantly affects the coalbed's effective stress, residual pressure after extraction, and the flow state of coalbed methane. The initial gas pressure in coal mines (x_1) typically ranges between 1 and 3 MPa. However, as mining depth increases, the gas pressure in coal seams also rises. Therefore, this study sets the gas pressure at four different levels: 1, 2, 3, and 4 MPa. Initial permeability (x_2) refers to the capacity of the coal seam rock or coal mass to allow gas or liquid to pass through under a given pressure difference before gas extraction. Permeability in coal seams varies widely, generally ranging from 1×10^{-17} to 1.0×10^{-14} m^2. However, coal seams with high gas extraction demands, particularly those with outburst risks, typically exhibit lower permeability. Previous studies have shown that permeability values below 2.5×10^{-17} m^2 are highly prone to gas outbursts. Yet, based on previous fieldwork, coal seams with permeability between 3 and 4×10^{-17} m^2 are also considered to present significant outburst risks. Therefore, in this study, the permeability of coal seams is set to four different values: 1, 2, 3, and 4 ($\times 10^{-17}$ m^2). Extraction time x_3 is the duration of the gas extraction process, directly affecting the total amount of methane extracted and the effectiveness of the extraction. In coalbed methane extraction operations, the time required to achieve the target extraction standard directly impacts the production continuity of the mining face. Therefore, the extraction time was varied over a range of 1, 10, 20, 30, . . ., and 300 days to comprehensively cover different stages of coalbed methane extraction.

A full-order numerical model for coal mine gas extraction was computed based on the cross-combination of different parameters, yielding results for the distribution of coal seam gas pressure, gas extraction flow rate x_4, and gas extraction concentration x_5. A total of 480 experimental samples were generated. Prior to model training and optimization, these samples were divided into training and testing sets in a 9:1 ratio and subsequently standardized.

3.2. Hyperparameter Tuning of Reconstructed Pressure Field Models for Coal Seam Gas Extraction

This subsection employs mean squared error (MSE) as the evaluation metric to perform hyperparameter tuning for the convolutional autoencoder model using grid search. The grid search results are depicted in Figure 7. The x-axis represents different learning rates (lr), ranging from 0.005, 0.003, 0.001, 5 × 10^{-4}, 1 × 10^{-4}, 5 × 10^{-5}, to 1 × 10^{-5} from left to right. The y-axis denotes different batch sizes, ranging from 128, 96, 64, 32, 16, 8, to 4 from top to bottom. The color bar transitions from red (high error) to blue (low error), with darker colors indicating higher errors.

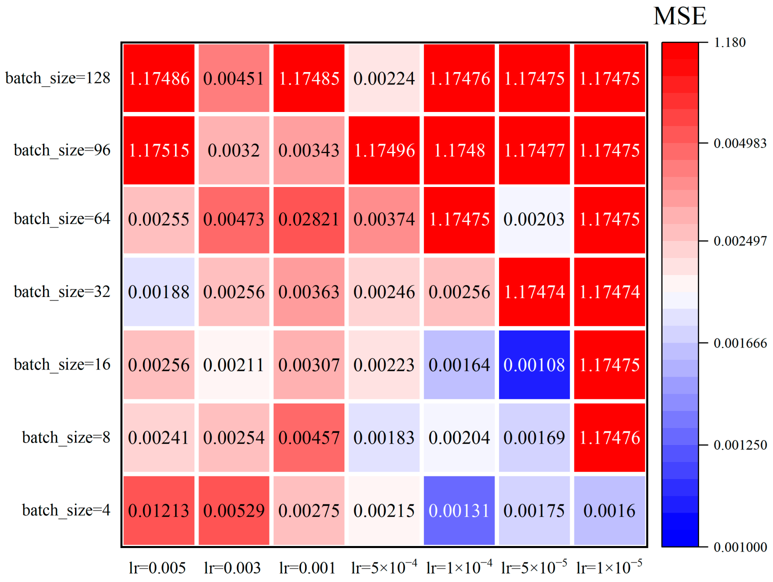

	lr=0.005	lr=0.003	lr=0.001	lr=5×10^{-4}	lr=1×10^{-4}	lr=5×10^{-5}	lr=1×10^{-5}
batch_size=128	1.17486	0.00451	1.17485	0.00224	1.17476	1.17475	1.17475
batch_size=96	1.17515	0.0032	0.00343	1.17496	1.1748	1.17477	1.17475
batch_size=64	0.00255	0.00473	0.02821	0.00374	1.17475	0.00203	1.17475
batch_size=32	0.00188	0.00256	0.00363	0.00246	0.00256	1.17474	1.17474
batch_size=16	0.00256	0.00211	0.00307	0.00223	0.00164	0.00108	1.17475
batch_size=8	0.00241	0.00254	0.00457	0.00183	0.00204	0.00169	1.17476
batch_size=4	0.01213	0.00529	0.00275	0.00215	0.00131	0.00175	0.0016

Figure 7. Mesh search results for model batch size and learning rate for CAE.

The combination of batch size = 16 and learning rate = 5 × 10^{-5} yields the lowest MSE of 0.00108. Generally, smaller batch sizes (4~32) and smaller learning rates (1 × 10^{-5}~1 × 10^{-4}) result in lower MSE values and provide more stable performance. When the batch size is smaller (4~32), the model's MSE tends to perform better. Performance significantly deteriorates when the batch size increases to 64 or above. For example, when batch size = 128 and learning rate = 0.005, the model exhibits poor performance (MSE = 1.17486). With larger batch sizes (such as 128 or 96), regardless of learning rate adjustments, the MSE values remain high. Conversely, smaller batch sizes (such as 4, 8, or 16) result in a significant decrease in MSE, particularly when paired with smaller learning rates.

Additionally, the model performs better with smaller learning rates (1 × 10^{-5} to 1 × 10^{-4}) during optimization. Learning rates greater than 0.001 cause the model to fail in effectively learning, leading to a sharp decline in performance and MSE approaching 1.17. Larger learning rates (such as 0.005 or 0.003) generally result in higher MSE values.

Smaller learning rates (such as 1 × 10^{-4}, 5 × 10^{-5}, or 1 × 10^{-5}) significantly reduce MSE, especially when combined with smaller batch sizes. While smaller learning rates and batch sizes improve MSE performance, they may increase the training time. Therefore, a balance between performance and efficiency should be considered in practical applications.

Based on the grid search tuning results, the convolutional autoencoder was trained using the parameter combination of batch size = 16 and learning rate = 5 × 10^{-5}. Figure 8 illustrates the decline in MSE during the training process. The horizontal axis represents the number of training steps, while the vertical axis denotes the MSE value. The training process is generally divided into four stages. (1) Initial high error: at the start of training, the initial MSE is close to 1, indicating a large prediction error from the model in its initial state. (2) Rapid decline phase: within the first 50 steps, the MSE value decreases rapidly. This swift reduction in initial error occurs because the model begins to capture the fundamental patterns and features in the data. This phase represents a quick transition from the model's random initialization state to a basic understanding of the data. The learning rate of 5 × 10^{-5} performs well during this early phase, without exhibiting oscillations or convergence issues that might occur with a higher learning rate. (3) Slow decline phase: after approximately 50 steps, the rate of MSE reduction slows significantly, and the curve flattens out. This indicates that the model has gradually reached a lower error level, with the smaller learning rate leading to smaller adjustment steps. (4) Stabilization: in the later stages of training (around 200 steps and beyond), the MSE value stabilizes with minimal changes, and the curve becomes nearly horizontal. This suggests that the model is nearing convergence, with its performance stabilizing and the error no longer significantly decreasing.

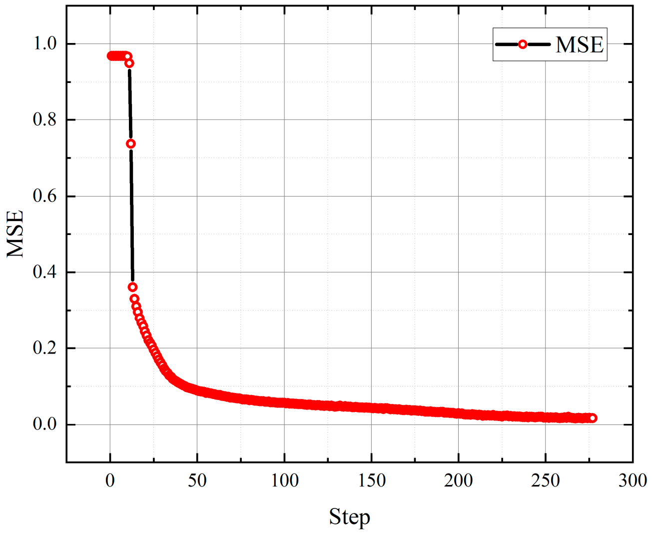

Figure 8. Learning error of CAE decreases when batch_size = 16 and lr = 5 × 10^{-5}.

The results indicate that the chosen batch size (16) and learning rate (5 × 10^{-5}) are effective, bringing the model close to a global optimal state while avoiding the slow learning progress that can occur with excessively low learning rates.

Figure 9 illustrates the reconstruction performance of the CAE model for the gas extraction pressure field, showcasing exceptional accuracy. The reconstructed pressure field is visually indistinguishable from the real pressure field, indicating that the CAE effectively captures and reproduces the critical features of the pressure field. The CAE demonstrates a strong ability to preserve spatial structure, with both the central low-value regions and the surrounding high-value regions maintaining a high degree of consistency in terms of shape, size, and position compared to the full-order pressure field.

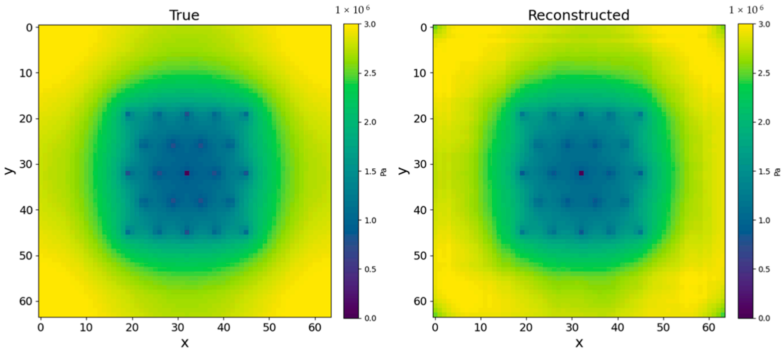

(**a**) $x_1 = 4.0$ MPa, $x_2 = 2.0 \times 10^{-17}$ m^2, $x_3 = 91.0$ d, $x_4 = 8.6\%$, $x_5 = 0.050$ m^3/min.

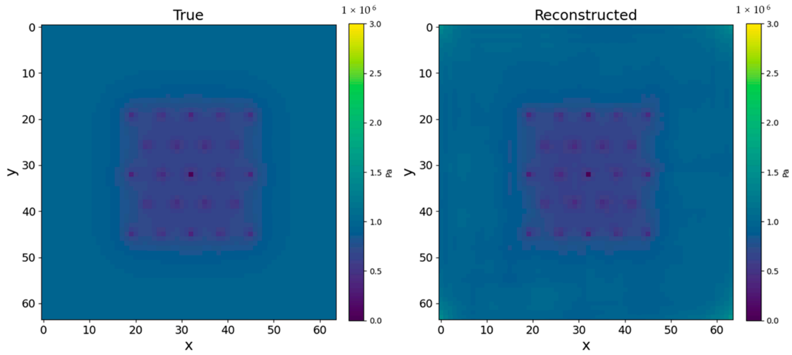

(**b**) $x_1 = 1.0$ MPa, $x_2 = 2.0 \times 10^{-17}$ m^2, $x_3 = 111.0$ d, $x_4 = 3.2\%$, $x_5 = 0.026$ m^3/min.

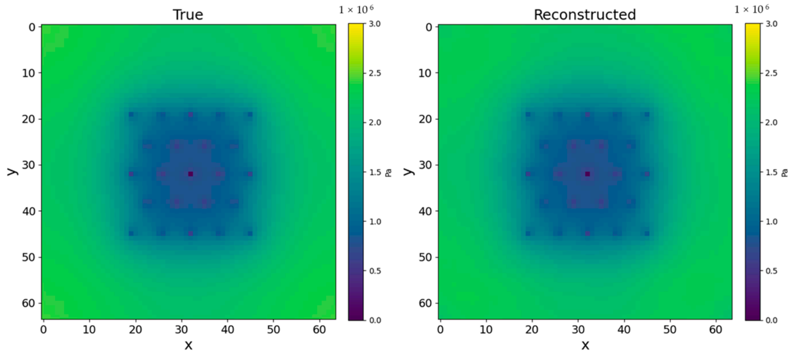

(**c**) $x_1 = 3.0$ MPa, $x_2 = 4.0 \times 10^{-17}$ m^2, $x_3 = 71.0$ d, $x_4 = 8.1\%$, $x_5 = 0.039$ m^3/min.

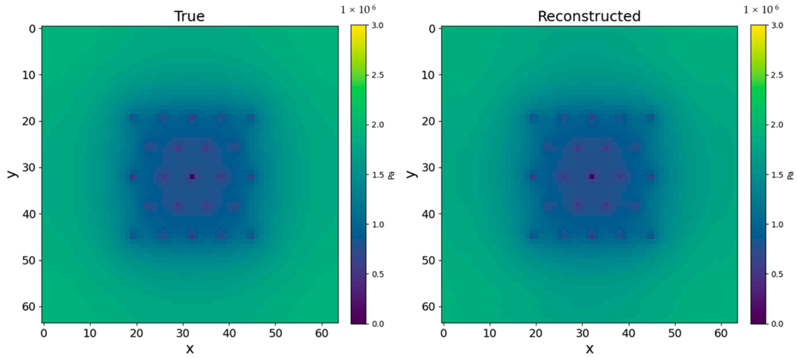

(**d**) $x_1 = 2.0$ MPa, $x_2 = 1.0 \times 10^{-17}$ m^2, $x_3 = 221.0$ d, $x_4 = 0.6\%$, $x_5 = 0.008$ m^3/min.

Figure 9. Effect of CAE on the reconstruction of the gas extraction pressure field.

The CAE also has a strong ability to capture nonlinear details. Even subtle changes in the flow field can be accurately reconstructed by the CAE. For example, it effectively models the sharp pressure gradients around gas extraction boreholes and the gradual transitions at the pressure field periphery. Moreover, the CAE handles pressure field boundaries delicately, without noticeable boundary distortion or blurring. From various reconstruction cases with different gas extraction parameters, it is evident that the CAE can accurately reconstruct pressure fields with varying gas pressures and distributions, demonstrating stability in handling diverse pressure field scenarios. The CAE model constructed in this study excels in overall pressure field reconstruction, detail preservation, adaptability to different pressure field patterns, and boundary handling. Its high-precision reconstruction capability provides a solid foundation for applications in pressure field prediction, parameter estimation, and real-time monitoring.

3.3. DNN Hyperparameter Tuning

Hyperparameter tuning for the batch size (batch_size) and learning rate (lr) of the DNN-based latent space parameter prediction model was conducted using grid search, with the results shown in Figure 10. Each cell displays the MSE under specific combinations of batch size and learning rate, with colors ranging from red to blue, indicating a range of error values from high (4.0200) to low (0.0460).

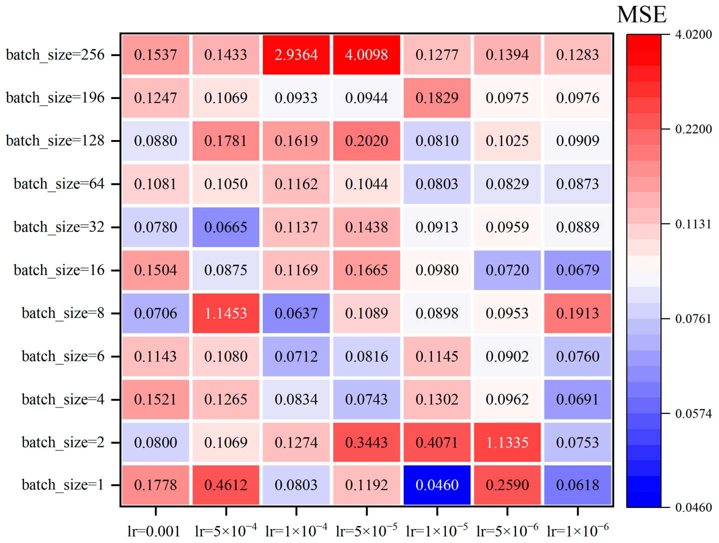

	lr=0.001	lr=5×10^{-4}	lr=1×10^{-4}	lr=5×10^{-5}	lr=1×10^{-5}	lr=5×10^{-6}	lr=1×10^{-6}
batch_size=256	0.1537	0.1433	2.9364	4.0098	0.1277	0.1394	0.1283
batch_size=196	0.1247	0.1069	0.0933	0.0944	0.1829	0.0975	0.0976
batch_size=128	0.0880	0.1781	0.1619	0.2020	0.0810	0.1025	0.0909
batch_size=64	0.1081	0.1050	0.1162	0.1044	0.0803	0.0829	0.0873
batch_size=32	0.0780	0.0665	0.1137	0.1438	0.0913	0.0959	0.0889
batch_size=16	0.1504	0.0875	0.1169	0.1665	0.0980	0.0720	0.0679
batch_size=8	0.0706	1.1453	0.0637	0.1089	0.0898	0.0953	0.1913
batch_size=6	0.1143	0.1080	0.0712	0.0816	0.1145	0.0902	0.0760
batch_size=4	0.1521	0.1265	0.0834	0.0743	0.1302	0.0962	0.0691
batch_size=2	0.0800	0.1069	0.1274	0.3443	0.4071	1.1335	0.0753
batch_size=1	0.1778	0.4612	0.0803	0.1192	0.0460	0.2590	0.0618

Figure 10. Mesh search results for model batch size and learning rate for DNN.

Regarding the impact of the learning rate on model MSE, Figure 10 indicates that higher learning rates (lr = 0.001 and 1 × 10^{-4}) tend to result in higher MSE values across most batch sizes. For instance, with batch_size = 256 and lr = 0.001, the MSE reaches 4.0098. This suggests that an excessively high learning rate may cause the model to overfit or become unstable, thereby failing to accurately capture the data features. Moderate learning rates (lr = 5 × 10^{-5} and 1 × 10^{-5}) generally result in lower MSE values, with the lowest MSE observed at batch_size = 1 and lr = 1 × 10^{-5}, where MSE is 0.0460. This range of learning rates appears to offer a good balance, allowing the model to learn effectively while maintaining stability. Conversely, lower learning rates (lr = 1 × 10^{-6}) often lead to increased MSE. For example, at batch_size = 8 and lr = 1 × 10^{-6}, the MSE is 1.1913. This indicates that excessively low learning rates can result in excessively slow learning, preventing the model from acquiring sufficient information effectively.

When the batch size during model training is larger (batch_size = 256, 196, 128), the model generally exhibits higher MSE. While a larger batch size provides stable gradient estimates, it may make it challenging for the model to escape local minima when combined with a higher learning rate. In contrast, a moderate batch size (batch_size = 64, 32, 16) tends to result in better MSE performance. For instance, with batch_size = 32 and a moderate learning rate lr = 5 × 10^{-5}, the model performs relatively well with an MSE of 0.0913.

Smaller batch sizes (batch_size = 8, 4, 2, 1) can also yield lower MSE values. For example, with batch_size = 1 and lr = 1 × 10^{-5}, the MSE is 0.0460. However, very small batch sizes can lead to higher MSE in certain combinations, such as batch_size = 8 and lr = 1 × 10^{-4}, which may be due to excessive gradient fluctuations. The lowest MSE is achieved with the combination of batch_size = 1 and lr = 1 × 10^{-5}. This indicates that under this configuration, the model can finely adjust to capture data features, resulting in the minimum error. Based on the hyperparameter tuning results, a batch size of 1 and a learning rate of 1 × 10^{-5} were chosen for training the DNN model. The trend of the MSE during training is illustrated in Figure 11, with the vertical axis using a logarithmic scale to depict the range of MSE values.

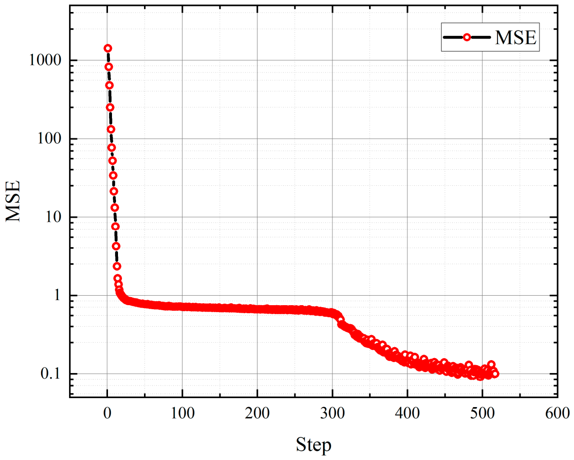

Figure 11. Decrease in learning error of DNN when batch_size = 1, lr = 1 × 10^{-5}.

Initially, the model exhibits a high MSE, reaching the thousands, as the parameters have not yet been adjusted and the prediction errors are substantial. However, within approximately the first 50 steps, the MSE rapidly declines, indicating that the model quickly learns the data features. In the intermediate phase, the MSE decreases more slowly, and the learning rate tapers off. A significant drop is observed around step 300, which may be attributed to the Adam optimization algorithm's adjustment of weights during the later stages of training. This adjustment, based on gradient information, effectively prevents the model from oscillating near local optima, facilitating further optimization. In the final phase, from step 300 to step 500, the model's mean squared error (MSE) continues to decrease, ultimately stabilizing at approximately 0.1.

4. Analysis

4.1. Performance Comparison

To validate the reliability and superiority of the DNN-CAE model reduction algorithm, this study compares its performance with the traditional POD-RBF model reduction algorithm using the same gas extraction pressure field dataset.

Figure 12 illustrates the reconstruction results of the true pressure field and the predictions obtained from the two methods: the DNN-CAE and POD-RBF. The DNN-CAE predictions are closer to the true pressure field, particularly in terms of the details and boundary regions of the pressure field. In contrast, the POD-RBF predictions show significant color discrepancies from the true pressure field, as seen in the low-value regions between boreholes in Figure 12a,b. This indicates that the DNN-CAE method achieves higher prediction accuracy compared to POD-RBF, which is further corroborated by the error results presented in Table 2.

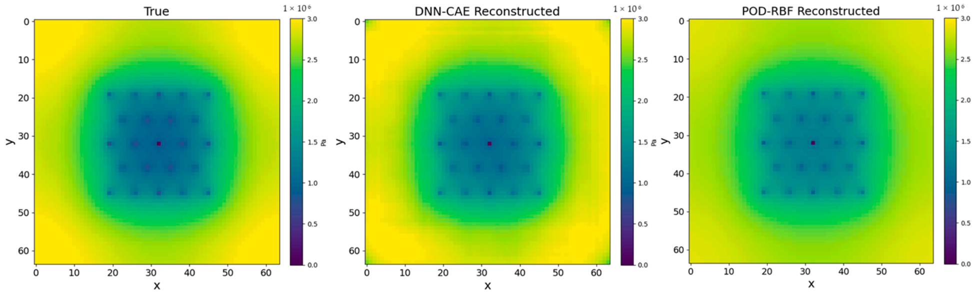

(**a**) $x_1 = 4.0$ MPa, $x_2 = 2.0 \times 10^{-17}$ m^2, $x_3 = 91.0$ d, $x_4 = 8.6\%$, $x_5 = 0.050$ m^3/min.

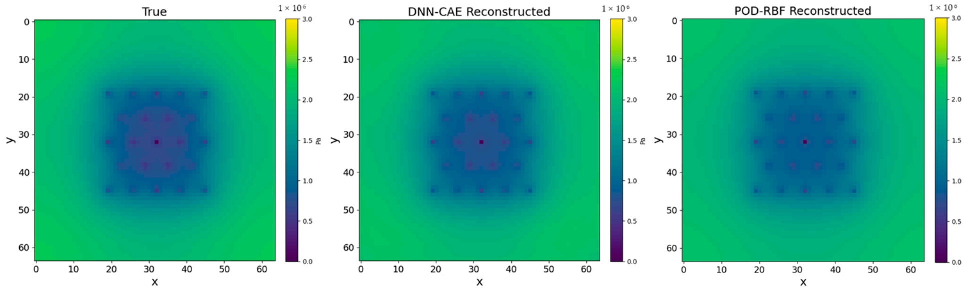

(**b**) $x_1 = 3.0$ MPa, $x_2 = 3.0 \times 10^{-17}$ m^2, $x_3 = 121$ d, $x_4 = 4.1\%$, $x_5 = 0.033$ m^3/min.

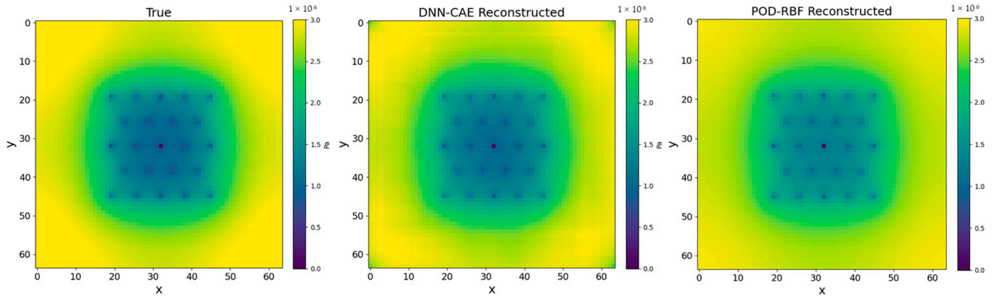

(**c**) $x_1 = 4.0$ MPa, $x_2 = 1.0 \times 10^{-17}$ m^2, $x_3 = 161$ d, $x_4 = 2.3\%$, $x_5 = 0.018$ m^3/min.

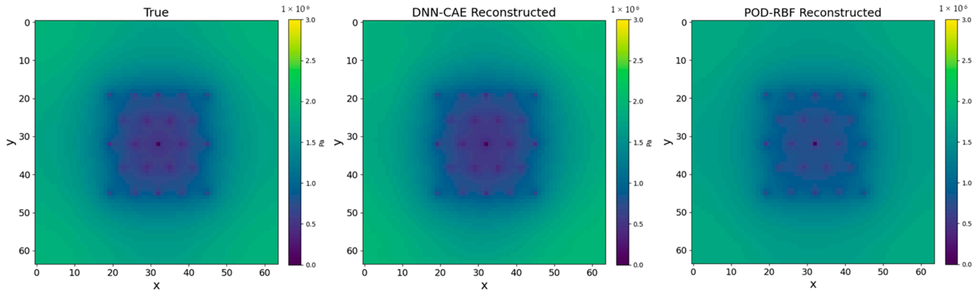

(**d**) $x_1 = 4.0$ MPa, $x_2 = 3.0 \times 10^{-17}$ m^2, $x_3 = 231$ d, $x_4 = 0.8\%$, $x_5 = 0.010$ m^3/min.

Figure 12. Comparison of the prediction effect of DNN-CAE and POD-RBF on the pressure field of gas extraction.

Moreover, the DNN-CAE method better preserves the overall structure and local features of the pressure field. For instance, in Figure 12c,d, the center low-value region reconstructed by the DNN-CAE closely matches the shape and size of the true pressure field. In contrast, POD-RBF exhibits some distortion, indicating that DNN-CAE has superior structural preservation capability. Additionally, the DNN-CAE effectively captures the extrema of the pressure field. For example, in Figure 12a,c, the high-value regions (yellow areas) reconstructed by the DNN-CAE are closer to the true pressure field compared to the POD-RBF method, which tends to underestimate these values. While DNN-CAE shows some unnatural artifacts in the boundary regions of the pressure field, it performs well in predicting key central borehole locations.

Table 3 further evaluates the predictive performance of the DNN-CAE and POD-RBF models using metrics such as mean squared error (MSE), mean absolute error (MAE), root mean squared error (RMSE), and reconstruction time. The comparison reveals that DNN-CAE outperforms POD-RBF across all performance indicators. Moreover, the DNN-CAE demonstrates significantly faster computational speed compared to POD-RBF. The prediction computation time for the DNN-CAE is under 1 s for all parameter combinations, while POD-RBF consistently exceeds 9 s. Specifically, with parameters (x_1 = 231.0, x_2 = 4.0, x_3 = 3.0), the DNN-CAE achieves a prediction time of 0.44761 s, while POD-RBF requires 10.01112 s, highlighting the DNN-CAE's substantial advantage in terms of computational efficiency.

Table 3. Comparison of prediction error and computation time between DNN-CAE and POD-RBF for gas extraction pressure field.

Values of Gas Extraction Parameters	**DNN-CAE**				**POD-RBF**			
x_1, x_2, x_3, x_4, x_5	**MSE**	**MAE**	**RMSE**	**Time**	**MSE**	**MAE**	**RMSE**	**Time**
4.0 MPa, 2×10^{-17} m^2, 91 d, 8.6%, 0.050 m^3/min	0.021	0.118	0.145	0.514	0.062	0.195	0.248	10.595
3.0 MPa, 3×10^{-17} m^2, 121 d, 4.1%, 0.033 m^3/min	0.006	0.058	0.080	0.636	0.025	0.124	0.159	10.312
4.0 MPa, 1×10^{-17} m^2, 161 d, 2.3%, 0.018 m^3/min	0.018	0.109	0.134	0.525	0.071	0.212	0.267	10.062
4.0 MPa, 3×10^{-17} m^2, 231 d, 0.8%, 0.010 m^3/min	0.003	0.044	0.055	0.448	0.019	0.106	0.138	10.011

This indicates that DNN-CAE not only provides higher accuracy but also faster computation speeds, demonstrating its broad potential for practical engineering applications.

4.2. Coal Mine Field Testing

To validate the field application effectiveness of the DNN-CAE reduced-order model for gas extraction pressure fields, the Ji$_{15\text{-}17}$-12130 mining face at Shoushan Mine in Xuchang City, Henan Province, China, was selected as the test site, as shown in Figure 13. This mining face is located in the seventh section of the eastern wing of the Ji-2 mining area, bordered by the Ji-2 mining area transport incline to the west and adjacent to the Mine 53 exploration line to the east. To the north lies the Ji$_{15\text{-}17}$-12110 mining face, which has already been mined, and to the south is the Ji$_{15\text{-}17}$-12150 gas control drift, currently under construction. The elevation of the mining face ranges from −797.1 m to −754.4 m, corresponding to a surface elevation of +136.4 m to +170.9 m. The designed strike length of the mining face is 1528 m, with a mining length of 271 m. The Ji$_{15\text{-}17}$ coal seam is being mined in this face, with an extractable reserve of 3.128 million tons. The Ji$_{15\text{-}17}$-12130 mining face has a uniform coal seam structure with relatively stable thickness. The Ji$_{15\text{-}17}$ coal seam is black, powdery, relatively soft, and fractured, with a banded structure, primarily consisting of bright coal, followed by dull coal and vitrain. The macroscopic coal lithotype is semi-bright coal, with a vitreous luster and a relatively soft texture. The coal seam thickness ranges from 4.9 to 6.5 m, averaging 5.3 m, with a relatively stable dip angle generally between 3° and 12°, averaging 7°.

The specific drilling operations for the Ji$_{15\text{-}17}$-12130 mining face (within the region extending 0–530 m outward from the cutting face) were carried out as follows, with the actual drilling layout presented in Figure 14.

Ji$_{15\text{-}17}$-12130 gas extraction tunnel No. 1: From 14 October 2022 to 15 April 2023, gas extraction drilling was conducted along the roadway direction in Gas Control Roadway No. 1. Drilling was performed every 6.4 m, with each group consisting of 16 hydraulic drilling holes. A total of 83 groups were drilled, comprising 1328 holes.

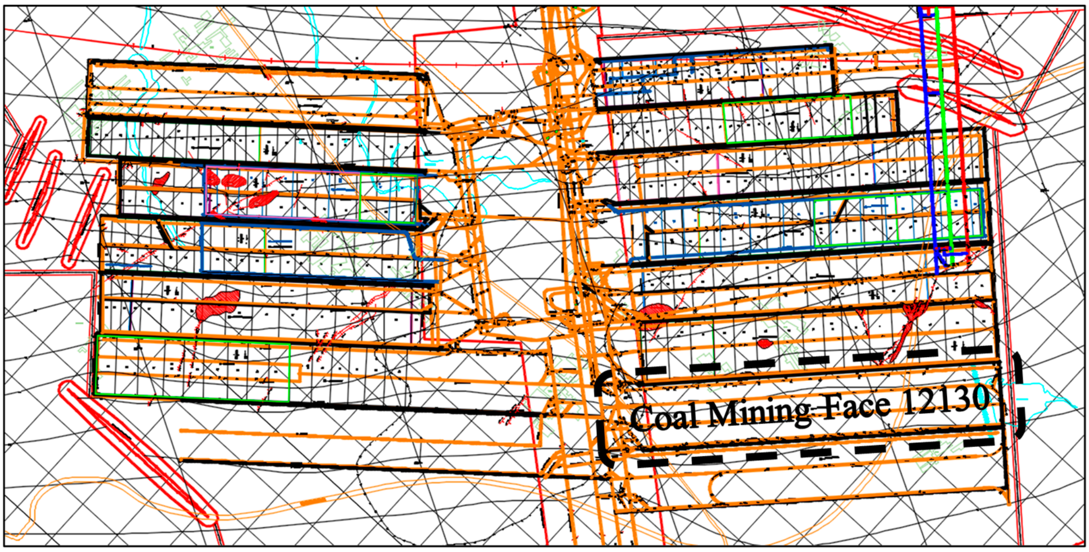

Figure 13. Plan view of mining and excavation projects in the Shoushan Mine area.

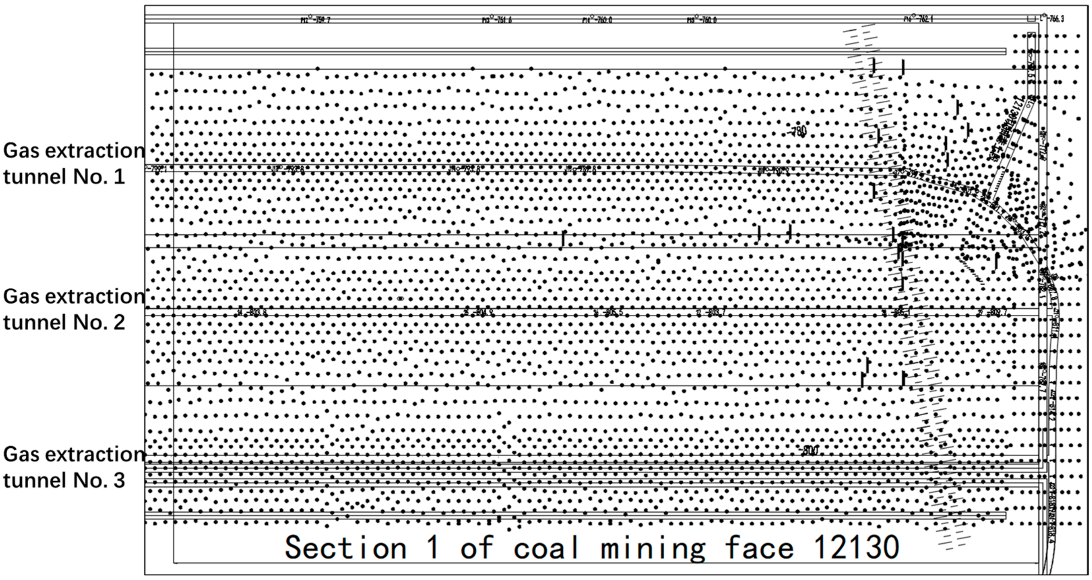

Figure 14. Plan view of borehole construction.

$Ji_{15\text{-}17}$-12130 gas extraction tunnel No. 2: From 27 December 2022 to 15 April 2023, gas extraction drilling was performed every 6.4 m, with each group consisting of 15 hydraulic drilling holes. The design called for 80 groups, totaling 1200 holes. However, based on actual field operations, a total of 81 groups were drilled, comprising 1215 holes.

$Ji_{15\text{-}17}$-12130 gas extraction tunnel No. 3: From 27 November 2022 to 15 February 2023, gas extraction drilling was conducted in the $Ji_{15\text{-}17}$-12130 machine roadway drainage. A total of 87 hydraulic drilling holes were completed along the roadway direction.

From the commencement of the first group of boreholes on 15 October 2022 until June 2023, a total of 1,743,026.2 m^3 of gas was extracted from the evaluation unit of the $Ji_{15\text{-}17}$-12130 mining face, extending 0–530 m outward from the cutting face. By the requirements for evaluating the effectiveness of anti-outburst measures, the residual gas pressure in the $Ji_{15\text{-}17}$-12130 mining face was directly measured from 15 June 2023 to 13 July 2023.

Figure 15 illustrates the distribution of gas pressure at various locations along the cut eye direction in the $Ji_{15\text{-}17}$-12130 mining face, as predicted using the DNN-CAE gas extraction pressure field reduced-order model. The variation in pressure is indicated by the color intensity. The accompanying table provides a detailed listing of the original gas pressure and the gas pressure after extraction for six measurement points. The last two columns present the actual gas pressure after extraction and the predicted gas pressure calculated using the DNN-CAE gas extraction pressure field reduced-order model.

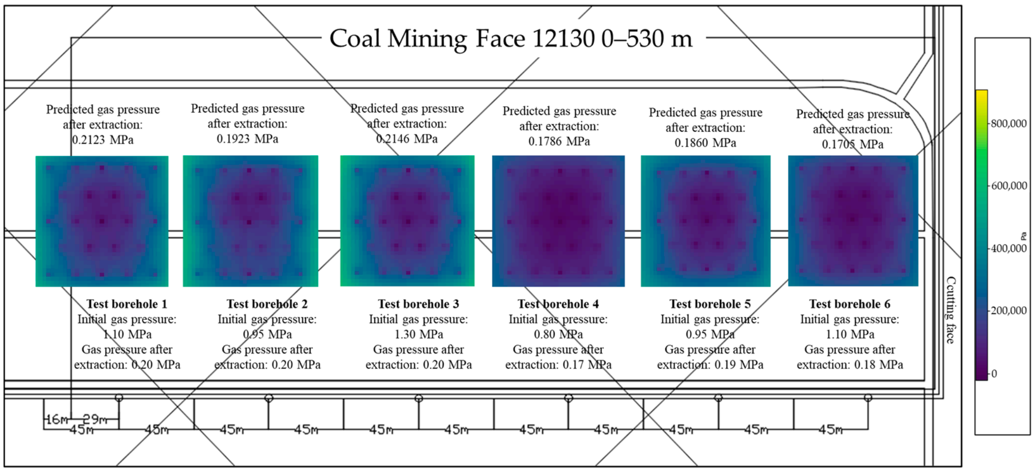

Figure 15. Distribution of test boreholes in the mining face and DNN-CAE reconstruction of the gas pressure field.

Table 4 presents the gas extraction parameters for the test boreholes and the residual coal seam gas pressure predicted using the DNN-CAE gas extraction pressure field reduced-order model. Combining the information from Figure 15 and Table 4, it is evident that within the 0 to 530 m range outward from the cutting face, the gas pressure exhibits a relatively uniform distribution. However, these values fluctuate due to the influence of extraction time as the distance increases. The gas extraction boreholes near the cutting face were drilled and extraction commenced earlier than those farther away. Consequently, the predicted gas pressures for test boreholes 1, 2, and 3, which are located farther from the cutting face, are higher than those for test boreholes 4, 5, and 6.

Table 4. Measured parameters of gas extraction in test boreholes and predicted gas pressure after extraction.

Test Boreholes	**Test Borehole 1**	**Test Borehole 2**	**Test Borehole 3**	**Test Borehole 4**	**Test Borehole 5**	**Test Borehole 6**
Test borehole location outside the cutting face	480 m	190 m	300 m	210 m	120 m	30 m
Initial gas pressure (MPa)	1.1	0.95	1.3	0.8	0.95	1.1
Initial coal seam permeability (10^{-17} m^2)	3	3	3	3	3	3
Extraction time (d)	150	140	140	170	160	180
Gas extraction flow rate (m^3/min)	0.051	0.060	0.055	0.046	0.052	0.046
Gas extraction concentration (%)	1.9	2.1	2.1	1.9	1.8	1.8
Actual gas pressure after extraction (MPa)	0.20	0.20	0.20	0.17	0.19	0.18
Predicted gas pressure after extraction (MPa)	0.2123	0.1923	0.2146	0.1786	0.1860	0.1705
MSE	2.73×10^{-5}					
MAE	0.00493					
RMSE	0.00522					

Based on Table 4, the DNN-CAE model performed well in predicting gas pressure after extraction in the $Ji_{15\text{-}17}$-12130 mining face of the Shoushan Mine. The MSE between the predicted and actual values is 2.73×10^{-5}, which is extremely low, indicating that the model's prediction errors are minimal across most measurement points. Since MSE is sensitive to larger errors, this suggests that the model demonstrates a high level of overall predictive accuracy. The MAE is 0.00493, representing the average absolute difference between predicted and actual values. A low MAE indicates that the DNN-CAE model's prediction error for gas pressure is approximately 0.005 on average, which is a very small margin of error, showcasing the model's strong predictive capabilities. The RMSE is 0.00522, slightly higher than the MAE. This is because RMSE is more sensitive to larger errors. Nevertheless, RMSE remains at a very low level, further affirming the model's high accuracy in predictions.

The DNN-CAE model's MSE, MAE, and RMSE values are all very small, indicating that its predictions for residual gas pressure in the test working face are highly accurate. Whether in terms of mean squared error, mean absolute error, or root mean squared error, this model fits the actual data well and demonstrates excellent predictive performance in the test working. The establishment of this model provides valuable insights for predicting residual gas pressure fields in coal mines.

5. Conclusions

(1) This paper proposes a reduced-order modeling method for coal mine gas extraction based on deep neural networks and convolutional autoencoders (DNNs-CAEs). The method encompasses five main components: full-order mathematical modeling, dataset construction, pressure field reconstruction model, and latent space parameter prediction model. The developed reduced-order model integrates both physical models and data-driven dynamics without explicit equations, enabling the effective prediction of reduced-order coal mine gas extraction pressure fields.

(2) A dataset for the numerical computation of the full-order gas extraction model pressure field was constructed. Hyperparameter experiments determined the optimal parameters for the pressure field reconstruction model and latent space parameter prediction model. The optimal parameters for the pressure field reconstruction model were found to be batch_size = 16 and lr = 5×10^{-5}, with the lowest MSE of 0.00108. The optimal parameters for the latent space parameter prediction model were batch_size = 1 and lr = 1×10^{-5}, achieving the lowest MSE of 0.046.

(3) To verify the reliability and superiority of the proposed DNN-CAE reduced-order algorithm, a comparative analysis was conducted between the DNN-CAE model and the traditional POD-RBF reduced-order model. The results demonstrate that DNN-CAE offers notable advantages over POD-RBF in terms of pressure field reconstruction accuracy, preservation of overall pressure field structure, and capture of pressure field extrema. Additionally, the DNN-CAE's computational time is consistently under 1 s, while POD-RBF exceeds 9 s. This indicates that DNN-CAE also possesses significant advantages in computational efficiency and holds considerable potential for practical applications in coal mining engineering.

(4) The $Ji_{15\text{-}17}$-12130 mining face at Shoushan Mine in Xuchang City, Henan Province, China, was selected as the test site. The DNN-CAE gas extraction pressure field reduced-order model was employed to predict gas pressure at various locations along the strike of the mining face. The MSE between the predicted values and the actual field measurements was 2.73×10^{-5}, the MAE was 0.00493, and the RMSE was 0.00522, indicating high accuracy in predicting gas pressure after extraction in the test working face. The establishment of this model provides valuable insights for predicting residual gas pressure fields in coal mines. We are also in the process of applying this model to a regional gas extraction digital twin system that we are developing.

Author Contributions: Conceptualization, T.H. and L.Z.; methodology, L.Z.; software, Y.D.; validation, F.L. and L.Z.; formal analysis, L.Z.; investigation, Y.T.; resources, Z.W.; data curation, X.L.; writing—original draft preparation, L.Z.; writing—review and editing, T.H.; visualization, Y.D.; supervision, T.H.; project administration, T.H.; funding acquisition, T.H. All authors have read and agreed to the published version of the manuscript.

Funding: We acknowledge the funding support from the National Natural Science Foundation of China (Nos. 52174174 and 52274193), Natural Science Foundation of Henan (No. 242300420025), Fundamental Research Funds for the Universities of Henan Province (No. NSFRF240804), the Special Program for Basic Research of Key Scientific Re-search Projects of Colleges and Universities in Henan Province of China (No. 21zx004), the Innovative Scientific Research Team of Henan Polytechnic University in China (No. T2022-1), the Visiting Scholar Foundation of Chongqing University in China (No. 2011DA105287-FW202102), Innovation Training Program for College Students in Higher Educational Institutions in Henan Province (Nos. 202311765050 and 2024117650200), Henan Province Housing and Urban-Rural Development Science and Technology Program (No. K-2310), and State Key Laboratory Cultivation Base for Gas Geology and Gas Control (Henan Polytechnic University) (No. WS2023B08).

Institutional Review Board Statement: Not applicable.

Informed Consent Statement: Not applicable.

Data Availability Statement: The raw data supporting the conclusions of this article will be made available by the authors on request.

Acknowledgments: The authors thank and extend their appreciation to the funders of this work.

Conflicts of Interest: The author declares no conflicts of interest.

References

1. Zhou, F.; Xia, T.; Wang, X.; Zhang, Y.; Sun, Y.; Liu, J. Recent developments in coal mine methane extraction and utilization in China: A review. *J. Nat. Gas Sci. Eng.* **2016**, *31*, 437–458. [CrossRef]
2. Liu, Y.; Du, Y.; Li, Z.; Zhao, F.; Zuo, W.; Wei, J.; Mitri, H. A rapid and accurate direct measurement method of underground coal seam gas content based on dynamic diffusion theory. *Int. J. Min. Sci. Technol.* **2020**, *30*, 799–810. [CrossRef]
3. Rong, T.; Liu, P.; Wang, J.; Ren, X.; Li, X.; Wang, G. Evolution of Permeability and Gas Seepage in Deep Coal Under 3D Stress. *Nat. Resour. Res.* **2024**, *33*, 765–791. [CrossRef]
4. Fu, C.; Xie, H.; Gao, M.; Wang, F.; Xie, J.; Liu, J.; Yang, B.; Tang, R. Mechanical behavior and seepage characteristics of coal under the loading path of roadway excavation and coal mining. *Geomat. Nat. Hazards Risk* **2021**, *12*, 1862–1884. [CrossRef]
5. Sun, X.; Hu, S.; Wu, X.; Chen, Z.; Zhang, Y.; Zhang, X.; Zhang, J. Permeability enhancement of coal-bearing propped fractures using blockage removal agent treatments in coalbed methane reservoirs. *Gas Sci. Eng.* **2024**, *124*, 205259. [CrossRef]
6. Dang, Z.; Wang, X.; Bie, S.; Su, X.; Hou, S. Experimental study of water occurrence in coal under different negative pressure conditions: Implication for CBM productivity during negative pressure drainage. *Energy* **2024**, *303*, 131989. [CrossRef]
7. Liu, Y.; Wang, E.; Li, M.; Song, Z.; Zhang, L.; Zhao, D. Mechanical response and gas flow characteristics of pre-drilled coal subjected to true triaxial stresses. *Gas Sci. Eng.* **2023**, *111*, 204927. [CrossRef]
8. Zhao, Y.; Liu, T.; Lin, B.; Jiang, B.; Zheng, C.; Zheng, Y.; Lu, K. Effect of stress evolution in a destressed borehole on gas desorption in deep coal seam. *Gas Sci. Eng.* **2024**, *128*, 205397. [CrossRef]
9. Wei, J.; Du, Y.; Liu, Y.; Zhao, L.; Wang, M.; Zhang, D.; Si, L.; Zhang, H. Experimental study on rock-breaking characteristics of advanced premixed abrasive water jet. *J. Chin. Inst. Eng.* **2024**, *47*, 508–519. [CrossRef]
10. Thomas, H.; Chen, M. Insights into carbon dioxide sequestration into coal seams through coupled gas flow-adsorption-deformation modelling. *J. Rock Mech. Geotech. Eng.* **2024**, *16*, 26–40. [CrossRef]
11. Mu, D.; Ma, Q.; Zhang, K.; Zhao, J. A gas-mechanical-damage coupling model based on the TLF-SPH method and its application to gas seepage in fractured coal. *Comput. Geotech.* **2024**, *171*, 106352. [CrossRef]
12. Ye, D.; Liu, G.; Gao, F.; Wen, L.; Wei, Z.; Li, D. Interdisciplinary approaches to modeling extraction efficiency and safety for clean energy under coupled multi-field effects. *Phys. Fluids* **2024**, *36*, 036624. [CrossRef]
13. Han, J.; Liu, Z.; Li, G.; Yang, H.; Hu, P.; Li, Z. Study of nonlinear gas transport in double-porous and double-permeable coal rocks based on the increasing fractal construction method. *Bull. Eng. Geol. Environ.* **2024**, *83*, 168. [CrossRef]
14. Qin, Y.; Fan, J.; Xu, H.; Li, Y.; Wu, F.; Li, W. Gas transport model and numerical solution in roof rock based on the theory of free gas diffusion. *Gas Sci. Eng.* **2024**, *124*, 205248. [CrossRef]
15. Gan, Y.; Wu, S.; Niu, D.; Liang, W. Multimechanism of Gas Transportation in Micro–Nanoscale Pores of Coal Seam: An Advanced Model of Gas Adsorption and Diffusion. *Energy Fuels* **2024**, *38*, 7899–7916. [CrossRef]
16. Xue, Y.; Liu, J.; Ranjith, P.G.; Liang, X.; Wang, S. Investigation of the influence of gas fracturing on fracturing characteristics of coal mass and gas extraction efficiency based on a multi-physical field model. *J. Pet. Sci. Eng.* **2021**, *206*, 109018. [CrossRef]

17. Wang, K.; Gong, H.; Wang, G.; Yang, X.; Xue, H.; Du, F.; Wang, Z. N2 injection to enhance gas drainage in low-permeability coal seam: A field test and the application of deep learning algorithms. *Energy* **2024**, *290*, 130010. [CrossRef]
18. Wei, J.; Du, Y.; Liu, Y.; Wang, M.; Zhao, L. The influence of pulse frequency on the energy evolution law and rock-breaking effect of pulsed abrasive water jet. *Phys. Fluids* **2024**, *36*, 043305. [CrossRef]
19. Kannapinn, M.; Schäfer, M.; Weeger, O. TwinLab: A framework for data-efficient training of non-intrusive reduced-order models for digital twins. *Eng. Comput.* 2024, *ahead-of-print*.
20. Coenen, D.; Oprins, H.; Degraeve, R.; Wolf, I.D. Benchmarking of Machine Learning Methods for Multiscale Thermal Simulation of Integrated Circuits. *IEEE Trans. Comput.-Aided Des. Integr. Circuits Syst.* **2023**, *42*, 2264–2275. [CrossRef]
21. Chen, G.; Qi, B.; Hu, W.; Zhang, Y.; Wei, J. A fast POD prediction method for hydrogen leakage at different pressures. *Int. J. Hydrogen Energy* **2024**, *49*, 1391–1404. [CrossRef]
22. Belhorma, M.; Bounab, B.; El Yousfi, B. Investigation of the Unbalance Estimation for a Double U-Joint Driveshaft Under Misalignment Uncertainty and Decreased Stiffness. *J. Vib. Eng. Technol.* **2024**, *12*, 1787–1798. [CrossRef]
23. Samuel, J.; Muggeridge, A.H. Non-Intrusive Reduced Order Modelling for the fast simulation of gas reservoirs. *J. Nat. Gas Sci. Eng.* **2022**, *101*, 104527. [CrossRef]
24. Zendaki, Y.; Cao, B.T.; Alsahly, A.; Freitag, S.; Meschke, G. A simulation-based software to support the real-time operational parameters selection of tunnel boring machines. *Undergr. Space* **2024**, *14*, 176–196. [CrossRef]
25. Rao, P.P. Inverse parameter estimation using compressed sensing and POD-RBF reduced order models. *Comput. Meth. Appl. Mech. Eng.* **2024**, *422*, 116820. [CrossRef]
26. Shen, X.; Du, C.; Jiang, S.; Sun, L.; Chen, L. Enhancing deep neural networks for multivariate uncertainty analysis of cracked structures by POD-RBF. *Theor. Appl. Fract. Mech.* **2023**, *125*, 103925. [CrossRef]
27. Shen, X.; Du, C.; Jiang, S.; Zhang, P.; Chen, L. Multivariate uncertainty analysis of fracture problems through model order reduction accelerated SBFEM. *Appl. Math. Model.* **2024**, *125*, 218–240. [CrossRef]
28. Zhang, S.; Yu, B.; Chen, L. Non-iterative reconstruction of time-domain sound pressure and rapid prediction of large-scale sound field based on IG-DRBEM and POD-RBF. *J. Sound Vib.* **2024**, *573*, 118226. [CrossRef]
29. Fang, H.; Sang, S.; Liu, S. Establishment of dynamic permeability model of coal reservoir and its numerical simulation during the CO2-ECBM process. *J. Pet. Sci. Eng.* **2019**, *179*, 885–898. [CrossRef]
30. Liang, B.; Zhang, M.T.; Pan, Y.S.; Wang, Y.J. The Experimental Researeh on the Effeet of Gas on Mechanieal Properties and Mechanieal Response of Coal. *Chin. J. Geotech. Eng.* **1995**, *17*, 12–18.
31. Zhang, J.; Roegiers, J.; Bai, M. Dual-porosity elastoplastic analyses of non-isothermal one-dimensional consolidation. *Geotech. Geol. Eng.* **2004**, *22*, 589–610. [CrossRef]
32. Fang, H.; Sang, S.; Liu, S. The coupling mechanism of the thermal-hydraulic-mechanical fields in CH4-bearing coal and its application in the CO2-enhanced coalbed methane recovery. *J. Pet. Sci. Eng.* **2019**, *181*, 106177. [CrossRef]
33. Liu, T.; Lin, B.; Fu, X.; Liu, S. A new approach modeling permeability of mining-disturbed coal based on a conceptual model of equivalent fractured coal. *J. Nat. Gas Sci. Eng.* **2020**, *79*, 103366. [CrossRef]
34. Li, S.; Qin, Y.; Tang, D.; Shen, J.; Wang, J.; Chen, S. A comprehensive review of deep coalbed methane and recent developments in China. *Int. J. Coal Geol.* **2023**, *279*, 104369. [CrossRef]
35. Lou, Z.; Wang, K.; Kang, M.; Zhao, W.; Wei, G.; Yue, J.; Yao, H. Plugging methods for underground gas extraction boreholes in coal seams: A review of processes, challenges and strategies. *Gas Sci. Eng.* **2024**, *122*, 205225. [CrossRef]